

Gravity-aware Grasp Generation with Implicit Grasp Mode Selection for Underactuated Hands

Tianyi Ko^{*†}, Takuya Ikeda^{*}, Thomas Stewart^{*}, Robert Lee^{*}, Koichi Nishiwaki^{*}

Abstract—To overcome the mechanical limitation of parallel-jaw grippers, in this paper, we present a gravity-aware grasp generation that supports both precision grasp and power grasp of underactuated hands. We propose a novel approach to generate a large-scale dataset with a gravity-rejection score and experimentally confirm that the combination of that score and classical success/fail binary classification is powerful: the former encourages stable grasps, such as power grasps or grasping the center of mass, while the latter rejects invalid grasps, such as colliding with other objects or attempting to grasp parts that are too large for the gripper. We also propose a rotation representation that is continuous on $SO(3)$ and considers the grasp’s physical meaning. Our simulation and real robot evaluation experiments demonstrate significant improvements from the baseline works, especially for heavy objects.

I. INTRODUCTION

Parallel-jaw grippers are widely adopted in both academia and industry thanks to their simplicity, and many machine-learning-based approaches assume them as the end effector. Their grasp capability, though, is fundamentally limited because the two parallel small contact surfaces are fragile against the torque around them. Even when the grasp force and the friction coefficient are sufficient, the combination of such rotation, compliance of contact surface, and tangential force results in a drift of contact point that causes grasp failure.

Two-fingered underactuated hands enable both precision grasps and more stable power grasps with minimum cost on the system complexity. This switchable grasp mode, though, makes the grasp generation harder, resulting in limited works explicitly considering the hands’ capability. In this work, we aim to extend the existing machine-learning-based approaches to support and leverage the capability of underactuated hands from both the data generation and network architecture direction. Specifically, our work is based on the work by Breyer et al. (VGN) [1] due to its applicability to our problem setting. We name our approach PowerVGN, with the following contributions:

- Propose a data generation pipeline where the grasps are evaluated with disturbance in multiple directions first, then the multi-dimensional disturbance-rejection score is projected to the gravity direction in the scenes.
- Propose to have two network heads for gravity-rejection score regression and success/fail classification, with the former encouraging power grasps while the latter



Fig. 1. Our PowerVGN prioritizes power grasps to stably grasp unevenly shaped objects (left image), while implicitly switching to precision grasp mode when tabletop (middle image) or obstacles (right image) prohibit power grasp.

rejecting collision. Provide qualitative analysis of their effect.

- Propose a grasp orientation representation based on the physical meaning of the basis vectors of a rotation matrix, which is continuous on $SO(3)$.
- Propose an evaluation protocol with variable objects’ weight and perform thorough ablation studies to show which parts are important for grasping.
- Provide a real-system evaluation to show the significant improvement of our approach quantitatively.

II. RELATED WORKS

In this work, we focus on learning-based 6-DoF grasp generation. Initial works on 6-DoF grasp generation include the one by Gualtieri et al. [2] where grasp candidates are heuristically sampled, and the partial point cloud cropped by the sampled grasp is fed into a learned classifier. Liang et al. [3] leveraged recent advances of PointNet [4] to improve the classifier part. While those works relied on a sample-then-classify scheme, Qin et al. [5] proposed to predict per-point scoring and grasp rotation in a single forward path, which drastically reduced the inference time and omitted a hand-crafted sampling algorithm. Our approach also belongs to this line of work that batch-infers the grasp metrics and rotations for all voxels.

There are two major approaches to the input/output design of the network: (i) using point cloud as the scene expression and PointNet-based [4], [6] architecture to process the feature of points on the object’s surface, then using one or more key points to reconstruct the grasp pose, and (ii) using a volumetric approach such as TSDF [7] with a fully-convolutional architecture. In the context of the former case,

^{*} T. Ko, T. Ikeda, T. Stewart, R. Lee, K. Nishiwaki are with Woven by Toyota, Inc., 3-2-1 Nihonbashi-Muromachi, Chuo-ku, Tokyo, Japan.

[†] Corresponding author. tianyi.ko@woven.toyota

Qin et al. [5] regressed the translational offset from the key point and rotation. Cai et al. [8] took a similar approach with [5], but instead of directly regressing the rotation, they used a set of predefined discretized rotations to avoid rotation ambiguity. While [5], [8] directly handled the hand’s pose, Zhao et al. [9] assumed the key point as the contact point and regressed other properties, such as the other contact point’s location to reconstruct the grasp pose. Similarly, Sundermeyer et al. [10] regressed the hand’s contact direction and approach direction, assuming the key point is the contact point. Huang et al. [11] used two key points and surface normals to reconstruct grasp poses.

For the latter case, Breyer et al. [1] performed a 3D fully convolutional network on the TSDF volume to regress per-voxel score and rotation. Jiang et al. [12] also used the combination of TSDF and 3D-conv, but they trained an implicit expression where the network took the location as the query and returned the score and rotation. Winkelbauer et al. [13] also adopted the volumetric representation, but they used auto-regression to generate grasps with an anthropomorphic hand. Our work follows this line, especially close to [1], but with contributions described in section I that enabled automatic selection of the best grasp mode considering the gravity direction and scene collision.

III. SYNTHETIC DATA GENERATION TAKING ACCOUNT OF EXTERNAL DISTURBANCE FORCE REJECTION

A. Geometry-based Initial Grasp Sampling

Our work targets the category of hands with both precision grasp and power grasp capabilities. For precision grasps, we can efficiently find antipodal grasps [14] by sampling points on the mesh surface and computing its normal. Specifically, we first sample n points $\mathbf{p}_i \in \mathbb{R}^3, i = \{1 \dots n\}$ on the mesh surface. Denoting the normal at \mathbf{p}_i as $\mathbf{n}_i \in \mathbb{R}^3$ and $\mathbf{n}_{(i,j)} = (\mathbf{p}_j - \mathbf{p}_i) / \|\mathbf{p}_j - \mathbf{p}_i\|$, the counterpart point $\mathbf{p}_{\text{antipodal}}(i) = \mathbf{p}_j$ that construct the antipodal grasp can be acquired by the following max-min problem:

$$j = \underset{j \in \{1 \dots n\}}{\operatorname{argmax}} \min(\mathbf{n}_i \cdot \mathbf{n}_{(j,i)}, \mathbf{n}_j \cdot \mathbf{n}_{(i,j)}). \quad (1)$$

Since the antipodal pair does not contain rotation information, we rotate the hand around $\mathbf{n}_{(i,j)}$ with $\theta_k = 2(k/m)\pi, k = \{1 \dots m\}$. Finally, we get the hand’s base pose $\mathbf{T}_{(i,k)} \in SE(3)$ by solving the inverse kinematics of the hand because, for our target hand, the distance between the object and the palm varies according to the object’s size:

$$\mathbf{T}_{(i,k)} = \text{InverseKinematics}(\mathbf{p}_i, \mathbf{p}_j, \theta_k) \quad (2)$$

Unlike precision grasps, it is difficult to analytically generate grasp poses with power grasp mode because the reverse model of an underactuated parallel-link mechanism is non-trivial. Thus, we augment the precision grasp pose by applying heuristic offsets and let the following simulation process refine them. Letting $\mathbf{T}_{\text{aug},a} \in SE(3), a = \{1 \dots l\}$ representing a constant transform from the precision grasp

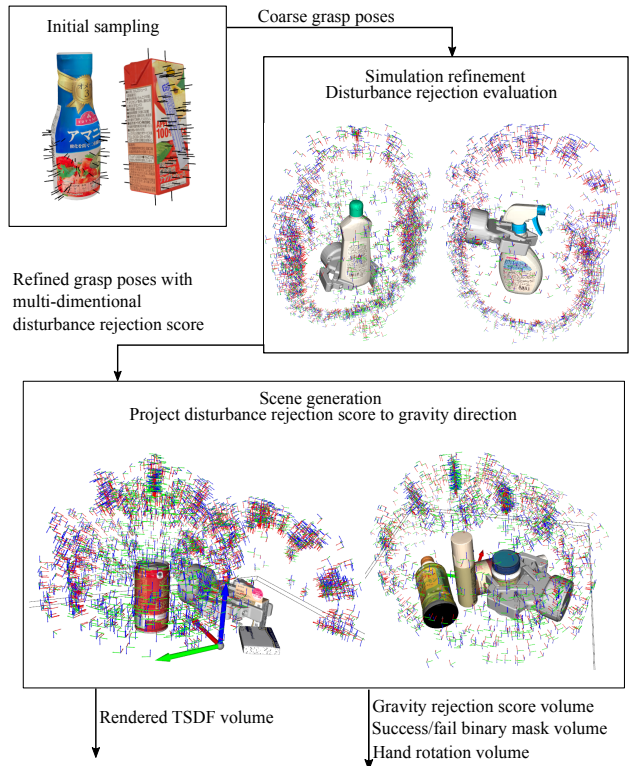


Fig. 2. Schematic of our data generation pipeline. We sample precision grasps based on the antipodal score and coarse power grasps by heuristically shifting the precision grasps (top-left). Those initial grasps are refined through grasp simulation (top-right). We apply external force in multiple directions and acquire a multi-dimensional disturbance-rejection score for each grasp. Finally, we create multi-object scenes and project per-object grasp poses to the scene to acquire the training data (bottom). The disturbance-rejection score is projected to the scene’s gravity direction to acquire the gravity-rejection score.

pose to the power grasp pose, the final grasp pose is represented by

$$\mathbf{T}_{(i,k,a)} = \mathbf{T}_{(i,k)} \mathbf{T}_{\text{aug},a} \quad (3)$$

In this work, we first sampled $n = 10000$ points on the mesh surface. Then, we iterate a process that samples one \mathbf{p}_i and get \mathbf{p}_j , rotate with $m = 12$, and finally apply $l = 3$ augmentation until we get 6000 grasps in total. The three \mathbf{T}_{aug} consist of an identity matrix, a translation matrix with 17.5 mm offset towards the object, and the other one with 25 mm. Note that these values are decided based on the mechanical property of the hand.

B. Simulation-based Grasp Evaluation and Refinement

While there are multiple analytical approaches to evaluate grasp quality [15], [16], they assume the contact points are given. Unlike parallel-jaw grippers, however, the contact points between the object and an underactuated hand are only decided after the physical interaction between the two occurs. Another difficulty in applying analytical approaches is that while they assume that a contact point can exert an arbitrary reaction force under the friction cone, underactuated hands have further constraints due to the parallel-link mechanism.

Winkelbauer et al. [13] extended the ϵ -quality with joint actuation torque constraints, but it was still limited to fully-actuated hands. Finally, while analytical approaches only handle static-friction region, how the object slips inside the hand matters: even when the contacts are identical, grasping a concave bottle-neck-shaped part is more robust than grasping a convex-shaped part when the static friction is broken and the object starts to slip. For underactuated hands, some failure modes are even beneficial, e.g., the object slips from a precision grasp mode to a more stable power grasp mode.

To fulfill our requirements, we run the full grasp process in a physics simulation. The hand and object are placed with a relative transformation $\mathbf{T}_{(i,k,a)}$ as defined in Eq. 3, without gravity. The hand closes from its fully-opened configuration until the fingers and the object’s position converge. Since the original hand-object transform is a rough estimate, we update it with the result after the simulation. Those grasps with initial collision or no hand-object contact are removed in this process.

In order to evaluate the grasp quality, we further apply external forces on the object’s center of mass until it slips out of the hand. Since robustness against an external disturbance force is dependent on the direction of that force, we apply external forces in multiple directions described in the hand’s frame and record the score for each direction.

For the simulator, we selected the one provided by Drake [17], whose hydroelastic contact model [18], [19] allows continuous surface contact modeling. We empirically found that continuous surface contact modeling is crucial for simulating grasps with underactuated hands since the point-contact model typically results in chattering due to the unstable loop between the contact point/force and closed-link mechanism dynamics. Another benefit is the support of non-convex non-watertight mesh, allowing us to directly use 3D scanned daily objects without tuning of convex decomposition parameters [20].

In this work, we scanned 75 daily objects as 3D meshes for our training data. Figure 2 top right shows examples of the refined grasp pose around the object. We selected the base vector of the hand frame ($\pm x, y, z$, see Fig. 3) as the external force directions, i.e., six scores per each grasp pose.

C. Scene Generation

Inspired by the work by Qin et al. [5], we took a two-staged data-generation approach: (i) grasp poses are evaluated for each individual object first, as described in the previous subsection, then (ii) projected to a multi-object cluttered scene, which drastically reduces the computation time. In order to convert the multi-dimensional external force rejection scores to the scalar value, we projected them to the scene’s gravity direction. Denoting \mathbf{n}_i as the unit vector in whose direction we applied the external force (in the scene frame) and f_i as the maximum force the grasp can support in that direction, the grasp score at that grasp is defined as follows:

$$\min_{\{i|\mathbf{n}_i \cdot \mathbf{g} > \epsilon\}} \frac{f_i}{\mathbf{n}_i \cdot \mathbf{g}} \quad (4)$$

where $\mathbf{g} \in \mathbb{R}^3, |\mathbf{g}| = 1$ is the direction of gravity and ϵ is a small positive value.

To generate a scene, we first randomly sample the number of objects from $\{1\dots 5\}$, then randomly select their class and position. In our daily lives, we frequently encounter cylinder-shaped objects such as bottles with standing configurations. Randomly selecting their pose, though, results in most of them being laid down. In order to make the scene more realistic, we sample the rotation from two groups: in the former case, the rotation is randomized only around the gravity direction, while in the latter case, it is randomized in all directions. Simulation is performed until all objects are at rest, at which point the grasp poses of each object are projected to the scene space, and those in collision are removed.

In this work, we created 5K scenes with 14K objects and 6M grasps in total. Figure 2 bottom illustrates examples of the grasp poses projected to the scene.

IV. GRASP REPRESENTATION AND NETWORK ARCHITECTURE

As the grasp representation, we follow the volumetric approach proposed by Breyer et al. (VGN) [1], where the depth images are integrated as TSDF [7] volume and a 3D fully convolutional network is used to generate grasp quality and rotation at each voxel. While the ease of using multiple depth images from multiple viewpoints is an advantage of TSDF expression, in this work, we focus on a single-camera setting for the sake of system simplicity, unlike the original work.

One critical contribution is the introduction of two separate heads, one for gravity-rejection score regression and the other for success/failure binary classification. The original VGN, on the contrary, only has a single grasp-quality head where all grasps exceeding the threshold are treated as the same, and another sampling logic, e.g., taking the one with the highest geometric location, is used. Our assumption is that the grasp success/fail label in the simulator cannot strictly coincide with the reality due to the sim-to-real gap; thus, we should always take the most promising one. This is especially the case for hands with both precision and power grasp capability because even if both grasp modes were successful in the simulator, we should take the latter because it is more robust as long as there are no other constraints, such as collision. In this work, we trained the network with the L2 loss to regress the gravity-rejection score described in the previous section.

Despite the introduction of the gravity-rejection score regression head, we still keep the binary classification head to filter out invalid grasps. Even though power grasps are advantageous in robustness, they are frequently prohibited due to collision with the table or other objects. Our hypothesis is that since such collision avoidance is a discontinuous function while the grasp quality should be a continuous one, separating them as different heads are advantageous in training. Another advantage is that since the gravity-rejection

score head is only trained on the valid grasp poses, the out-of-domain region, e.g., areas far away from the objects, needs to be removed. While the original VGN uses heuristic-based post-processing to remove those regions, our classifier can be trained to perform the equivalent filtering. In this work, we label the voxel as *success* if any grasp poses in the training data correspond to the voxel, and *fail* otherwise, with the cross-entropy loss.

A disadvantage of the volumetric approach is its sensitivity to the rotation error. Since the key voxel representing the grasp is distant from the object’s surface, a small rotation regression error may result in a large variation in the contact. It is known that rotation matrix representation is advantageous against quaternion representation since quaternion representation is discontinuous and difficult for neural networks to learn [21]. In addition to switching to rotation matrix representation from the original VGN’s quaternion representation, we hypothesize that some basis vectors are easier to learn compared with other directions. Specifically, we assume that the hand approach direction is the easiest one because it typically coincides with the direction from the key voxel to the closest point on the object’s surface. We assume the normal of the plane in which the finger moves is the secondary easiest direction, as it typically coincides with the principal axis of the object’s curvature. Defining the Tool Center Point (TCP) coordinate as Fig. 3, the rotation matrix is reconstructed by $\mathbf{R} = [\mathbf{e}_x \ \mathbf{e}_y \ \mathbf{e}_z]$:

$$\begin{aligned} \mathbf{e}_x &= \frac{\tilde{\mathbf{e}}_x}{|\tilde{\mathbf{e}}_x|} \\ \mathbf{e}_z &= \frac{\mathbf{e}'_z}{|\mathbf{e}'_z|}, \quad \mathbf{e}'_z = \tilde{\mathbf{e}}_z - (\mathbf{e}_x \cdot \tilde{\mathbf{e}}_z)\mathbf{e}_x \\ \mathbf{e}_y &= \mathbf{e}_z \times \mathbf{e}_x \end{aligned} \quad (5)$$

where $\tilde{\mathbf{e}}_x \in \mathbb{R}^3$ and $\tilde{\mathbf{e}}_z \in \mathbb{R}^3$ are the network output. We used the cosine-similarity loss for the two vectors and took the absolute value for the case of $\tilde{\mathbf{e}}_z$ to handle the hand’s symmetry ambiguity.

V. EXPERIMENT AND EVALUATION

A. Qualitative Analysis of Network Output

In order to inspect the network output, we placed two primitive objects in the simulator: a 65-mm-diameter, 200-mm-tall cylinder at $[-0.0325, 0, 0]$ [m] location and a 100-mm-sized cube at $[0.06, 0, 0]$ [m] location. Even though these two objects were not included in our dataset, their geometries fall into our typical cases, such as water bottles and daily goods boxes, because we target home-use products. We placed a single camera at $[0.5, 0, 0.5]$ [m] and analyzed the input TSDF volume and output grasp volume. See Fig. 3 for the experiment scene.

Figure 4 shows a cross-section at $z = 0.15$ plane. We overlay the objects’ shapes on the figures to help the readers understand the scene. Input TSDF volume (shown in the left figure) is not symmetrical around the cylinder because it is rendered from only one camera. Nevertheless, the output grasp volume on the right figure is highly symmetrical,

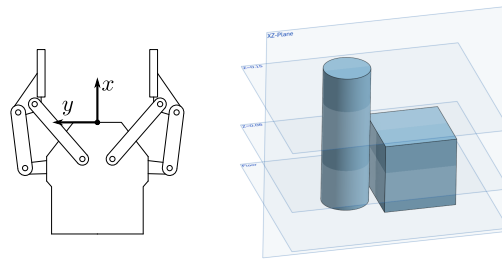


Fig. 3. TCP coordinate definition (left) and scene for the static network input/output analysis (right.) A 65-mm-diameter, 200-mm-tall cylinder and a 100-mm-sized cube are placed on the surface and the input/output of the network is visualized with the three blue-colored cross-sections.

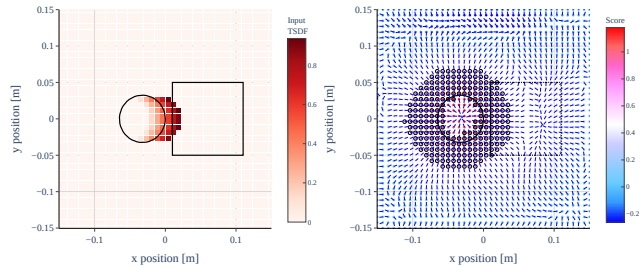


Fig. 4. Input TSDF volume (left) and output grasp volume (right) with $z = 0.15$ cross-section. The markers with black-circle are voxels with positive classification. The short blue lines are the hand approach direction.

implying that the network successfully learned shape completion. In the right figure, the color represents the grasp score at each voxel grid. The markers surrounded by a black circle are those with higher label values than the threshold, i.e., valid grasps. The blue short line from each marker is a projection of the approaching direction (\mathbf{e}_x in Fig. 3) on the cross-section plane.

Figure 4 illustrates the benefit of our approach in separating the score regression and label classification. The former is a continuous function, which takes a high value when the hand is close to the object. This is reasonable and desirable because a close distance has a high chance of resulting in a power grasp, while a far distance will result in a precision grasp. The problem is that this score takes a high value even inside the object, but those invalid grasps are filtered out by the latter label classification mask. Note that in our case, we take the TCP as a point on the hand’s palm (see Fig. 3); thus, the coincidence of classification boundary and objects’ boundary is physically reasonable.

Figure 5 shows a case with $z = 0.08$ [m] plane cross-section. As the left TSDF volume shows, at this height, the cylinder is almost invisible to the camera due to the occlusion by the cube. Nevertheless, the network still outputs valid grasps on the other side of the cylinder from the camera and cube. This suggests that the shape completion is performed based on a global context since the cylinder is only visible on its top side. Another insight is that the label classification is also effective for filtering out cases where the object is too big for the hand. In the figure, approaching from y-direction is invalid because the hand cannot open that wide. We can

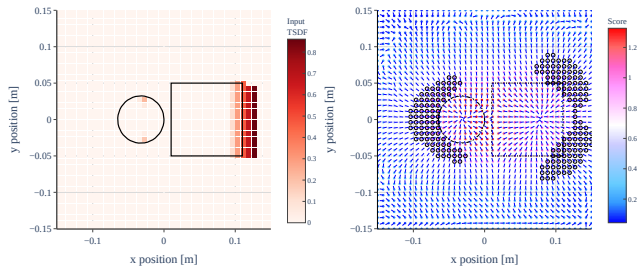


Fig. 5. Input TSDF volume (left) and output grasp volume (right) with $z = 0.08$ cross-section. The score prioritizes power grasp while the classification rejects grasps with collision or with too-big width.

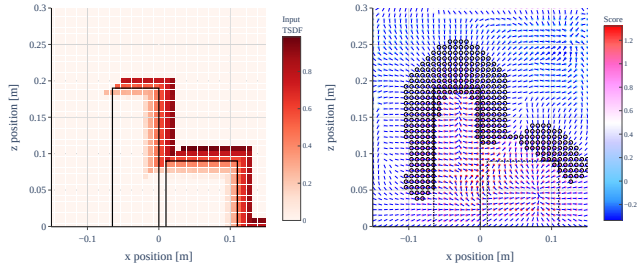


Fig. 6. Input TSDF volume (left) and output grasp volume (right) with $y = 0$ cross-section. Even for the region invisible to the camera, the network well predicts grasp poses. The classification properly removes grasps where the palm may collide with other objects.

see that while the score is still high for such regions, they are masked by the label classification.

Figure 6 shows another case with $y = 0$ [m] plane. In this case, the regions between the cylinder and the cube, and the region around $x = 0.03, y = 0.11$ [m] point are also filtered out by the label classification mask, even though they have high gravity-rejection scores. This masking is indeed valid because the hand’s base will collide with other objects in this region, proving that the label classification is also effective in collision avoidance.

B. Ablation Study with Physics Simulation

1) *Experiment Protocol*: In order to perform a fair comparison with our baseline, we utilized the mesh models provided by Breyer et al. [1] which are also used by other works [11], [12]. Following other works [1], [5], [8], [9], [11], [12], we also use the same two metrics for the evaluation: success ratio (SR) representing the number of successful grasps divided by the number of total trials, and clear ratio (CR) representing the number of successful grasps divided by the total number of objects. Each scene is terminated after two consecutive grasp failures or detection failures. We generated 128 scenes based on the process described in III-C and kept using the same scenes for all the simulation experiments.

2) *Evaluation Against Multiple Object Weight*: Since the success of grasp heavily depends on the object’s physical properties, we evaluate the grasps with multiple object weights and plot the success ratio and clear ratio against the objects’ weight in Fig. 7. Case 1 (blue) represents the

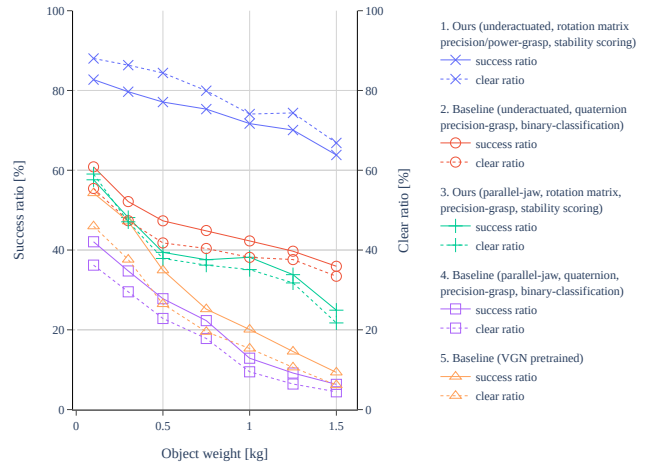


Fig. 7. Success ratio (SR) and clear ratio (CR) against multiple object weights. Scenario 1/2 are the case of the underactuated hand, while scenario 3/4/5 are with the parallel-jaw gripper. Scenario 1/3 uses vector rotation representation and stability score, while Scenario 2/4 use quaternion and only binary classification. Scenario 5 is the pre-trained weight of VGN [1].

case with all our contributions: using the underactuated hand (Robotiq 2F-85), training dataset with power grasp and gravity-rejection score, and the physically-feasible vector rotation representation. Case 2 (red) represents our baseline. We use the same hand, but in the data-generation process, we omitted the augmentation for power grasp (Eq. 3). In the inference stage, we ignored the gravity-rejection score and only used the binary classification mask. Following the approach of [1], [2], we selected the grasp with the maximum height. In addition, we used quaternion as the rotation representation, as in the case of [1]. Case 3 (green) represents our approach adopted for Franka Emika’s default parallel-jaw gripper. Since the gripper does not support power grasp, we omitted the power grasp augmentation in Eq. 3. Notice that we made the hands’ properties, such as grasp force, friction, and hydroelastic contact parameters, identical for the two hands. Case 4 (purple) shows the case where our baseline (same as case 2) was adopted to the parallel-jaw gripper. Case 5 (orange) makes use of the pre-trained model weights provided by the authors of [1], which was trained on the parallel-jaw gripper and we used the same gripper for the evaluation.

The comparison between case 1 and case 2 shows a significant improvement in our approach. The difference is larger in the heavy object region, which is reasonable because power grasps are more effective when the object is heavy. Notice that the advantage is not limited to heavy objects because it means that we can reduce the grasp force for lighter objects, resulting in less chance of damage.

The comparison between case 4 and case 5 shows a limited performance gap, while case 5 slightly outperforms case 4. We assume the gap comes from (i) the authors of [1] making a better tuning than ours and (ii) the domain gap between training objects and test objects. Nevertheless, the small performance gap justifies our comparison between case

TABLE I
SUCCESS RATIO (SR) AND CLEAR RATIO (CR) UNDER DIFFERENT
ROTATION REPRESENTATION

	Rotation Matrix ($e_x \rightarrow e_z$)	Rotation Matrix ($e_y \rightarrow e_z$)	Quaternion
SR [%]	71.698	67.945	57.784
CR [%]	74.095	69.081	61.003

1 and case 2: even though we cannot directly compare our approach with the pre-trained one because of the different hand mechanisms, our baseline mimics the existing works well.

One additional insight comes from the comparison between case 3 and case 4/5: even though the hand does not support power grasps, our approach is still advantageous when the objects are heavy. We assume that it is because our approach prioritizes grasps close to the center of mass or close to geometries such as bottlenecks.

3) *Effect of Rotation Representation*: In order to clarify the effect of rotation expression on the performance, we fixed the objects' weight to 1 kg and performed the simulation with two rotation expressions: *vector* and *quaternion*. For the former case, we trained the network to output three basis vectors (e_x, e_y, e_z) and only used two of them to reconstruct a rotation matrix based on Eq. 5. Table I summarizes the result. On the leftmost is the case of our proposal: e_x as the primary vector and e_z as the second. (See Fig. 3 for the coordinate.) In the middle is the case where the rotation matrix is reconstructed by e_y - e_z order. On the rightmost is the case with quaternion expression.

While both cases of *vector* outperformed *quaternion*, the e_x - e_z approach outperformed the e_y - e_z approach by 3.7% in success rate and 5.0% in clear rate. This supports our hypothesis that taking a proper set of basis vectors and properly prioritizing them in the inference time is beneficial.

C. Evaluation with a Physical System

We selected nine kinds of objects from the YCB dataset [22] (see Fig. 8), which we didn't use for training, and performed an evaluation with the identical process to section V-B.2 in a system with Franka Emika's Panda [23] arm. Depth image was acquired from a pair of RGB cameras and a learning-based stereo inference [24].

We first created 20 scenes with 51 objects in total in the simulation, as in section III-C. In the real system, we overlaid the scene's mesh with the real-time-streamed point cloud and manually adjusted the objects' pose in the real world until the two matched in a 3D viewer. This process allows us to use identical configurations for multiple experiments, even though the scene is randomly generated. In order to prevent damage to the objects, we restricted the hand force to 100 N. During the experiments, the robot tried the inferred grasp poses with the score order and automatically fell back to the following one if the previous one failed due to motion error originating from the range-of-motion limit. In that case, the



Fig. 8. Objects used for the real robot evaluation and the view of the experiment. We selected nine objects from the YCB dataset and created the scenes with the simulator. At the beginning of each evaluation, we overlaid the scene's mesh and point cloud to manually initialize the objects' poses on the table.

grasp was not counted as a failure as long as the following grasp succeeded.

Figure 8 shows captures of the experiment, and Table II summarizes the result. The left column represents our approach (corresponding to scenario 1 in section V-B.2), and the right column is the case of our baseline (scenario 2). While the difference is smaller than in the case of simulation in Fig. 7, our approach still outperformed our baseline by 10%pt in SR and 14 %pt in CR. We assume the smaller difference comes from (i) the objects being too light (all YCB's bottles are vacant) for the comparison, (ii) due to the motion limit of the robot, the best grasp pose was not possible, and it fell back to the first feasible grasp, which has a lower score.

TABLE II
SUCCESS RATIO (SR) AND CLEAR RATIO (CR) IN THE REAL ROBOT
EVALUATION

	Ours (1)	Baseline (2)
objects	51	51
trials	51	48
success	38	31
SR [%]	74.510	64.583
CR [%]	74.510	60.784

VI. CONCLUSION

In this paper, we presented a gravity-aware grasp generation algorithm that supports both precision grasps and power grasps using underactuated hands. A classification head rejects invalid grasps such as those colliding with the environment or trying to grasp objects that are too large for the gripper. A gravity-rejection score head prioritizes grasps with power grasp configuration and those close to the center of mass. A vector-based rotation head prioritizes the basis vectors based on their physical meaning to achieve accurate hand orientation regression. For the training data, we first generated per-object grasp poses with disturbance-rejection score annotation by applying external force in multiple directions. We then created cluttered scenes and projected the multi-dimensional disturbance-rejection score to the gravity direction to annotate the gravity-rejection score. Our qualitative and quantitative evaluation with both the simulator and the real robot showed significant improvement over our baseline.

REFERENCES

- [1] M. Breyer, J. J. Chung, L. Ott, R. Siegwart, and J. Nieto, "Volumetric grasping network: Real-time 6 dof grasp detection in clutter," in *Proc. of Conf. on Robot Learning*. PMLR, 2021, pp. 1602–1611.
- [2] M. Gualtieri, A. Ten Pas, K. Saenko, and R. Platt, "High precision grasp pose detection in dense clutter," in *Proc. of IEEE/RSJ Int'l. Conf. on Intelligent Robots and Systems*. IEEE, 2016, pp. 598–605.
- [3] H. Liang, X. Ma, S. Li, M. Görner, S. Tang, B. Fang, F. Sun, and J. Zhang, "Pointnetgpd: Detecting grasp configurations from point sets," in *Proc. of IEEE Int'l. Conf. on Robotics and Automation*. IEEE, 2019, pp. 3629–3635.
- [4] C. R. Qi, H. Su, K. Mo, and L. J. Guibas, "Pointnet: Deep learning on point sets for 3d classification and segmentation," in *Proc. of the IEEE conf. on computer vision and pattern recognition*, 2017, pp. 652–660.
- [5] Y. Qin, R. Chen, H. Zhu, M. Song, J. Xu, and H. Su, "S4g: Amodal single-view single-shot se (3) grasp detection in cluttered scenes," in *Proc. of Conf. on Robot Learning*. PMLR, 2020, pp. 53–65.
- [6] C. R. Qi, L. Yi, H. Su, and L. J. Guibas, "Pointnet++: Deep hierarchical feature learning on point sets in a metric space," *Advances in neural information processing systems*, vol. 30, 2017.
- [7] B. Curless and M. Levoy, "A volumetric method for building complex models from range images," in *Proc. of the 23rd annual Conf. on Computer graphics and interactive techniques*, 1996, pp. 303–312.
- [8] J. Cai, J. Cen, H. Wang, and M. Y. Wang, "Real-time collision-free grasp pose detection with geometry-aware refinement using high-resolution volume," *IEEE Robotics and Automation Letters*, vol. 7, no. 2, pp. 1888–1895, 2022.
- [9] B. Zhao, H. Zhang, X. Lan, H. Wang, Z. Tian, and N. Zheng, "Regnet: Region-based grasp network for end-to-end grasp detection in point clouds," in *Proc. of Int'l. Conf. on Robotics and Automation*. IEEE, 2021, pp. 13 474–13 480.
- [10] M. Sundermeyer, A. Mousavian, R. Triebel, and D. Fox, "Contact-graspnet: Efficient 6-dof grasp generation in cluttered scenes," in *Int'l. Conf. on Robotics and Automation*. IEEE, 2021, pp. 13 438–13 444.
- [11] H. Huang, D. Wang, X. Zhu, R. Walters, and R. Platt, "Edge grasp network: A graph-based se (3)-invariant approach to grasp detection," *arXiv preprint arXiv:2211.00191*, 2022.
- [12] Z. Jiang, Y. Zhu, M. Svetlik, K. Fang, and Y. Zhu, "Synergies between affordance and geometry: 6-dof grasp detection via implicit representations," *arXiv preprint arXiv:2104.01542*, 2021.
- [13] D. Winkelbauer, B. Bäuml, M. Humt, N. Thuerey, and R. Triebel, "A two-stage learning architecture that generates high-quality grasps for a multi-fingered hand," in *Proc of IEEE/RSJ Int'l. Conf. on Intelligent Robots and Systems*. IEEE, 2022, pp. 4757–4764.
- [14] I.-M. Chen and J. W. Burdick, "Finding antipodal point grasps on irregularly shaped objects," *IEEE transactions on Robotics and Automation*, vol. 9, no. 4, pp. 507–512, 1993.
- [15] C. Ferrari and J. F. Canny, "Planning optimal grasps," in *Proc. of Int'l. Conf. on Robotics and Automation*, vol. 3, no. 4. IEEE, 1992, p. 6.
- [16] A. T. Miller and P. K. Allen, "Graspit! a versatile simulator for robotic grasping," *IEEE Robotics & Automation Magazine*, vol. 11, no. 4, pp. 110–122, 2004.
- [17] R. Tedrake and the Drake Development Team, "Drake: Model-based design and verification for robotics," 2019. [Online]. Available: <https://drake.mit.edu>
- [18] R. Elandt, E. Drumwright, M. Sherman, and A. Ruina, "A pressure field model for fast, robust approximation of net contact force and moment between nominally rigid objects," in *Proc. of Int'l. Conf. on Intelligent Robots and Systems*. IEEE/RSJ, 2019, pp. 8238–8245.
- [19] J. Masterjohn, D. Guoy, J. Shepherd, and A. Castro, "Velocity level approximation of pressure field contact patches," *IEEE Robotics and Automation Letters*, vol. 7, no. 4, pp. 11 593–11 600, 2022.
- [20] K. Mamou, E. Lengyel, and A. Peters, "Volumetric hierarchical approximate convex decomposition," in *Game Engine Gems 3*. AK Peters, 2016, pp. 141–158.
- [21] Y. Zhou, C. Barnes, J. Lu, J. Yang, and H. Li, "On the continuity of rotation representations in neural networks," in *Proc. of Conf. on Computer Vision and Pattern Recognition*. IEEE/CVF, 2019, pp. 5745–5753.
- [22] B. Calli, A. Singh, A. Walsman, S. Srinivasa, P. Abbeel, and A. M. Dollar, "The ycb object and model set: Towards common benchmarks for manipulation research," in *Procs. of Int'l. Conf. on Advanced Robotics*. IEEE, 2015, pp. 510–517.
- [23] S. Haddadin, S. Parusel, L. Johannsmeier, S. Golz, S. Gabl, F. Walch, M. Sabaghian, C. Jähne, L. Hausperger, and S. Haddadin, "The franka emika robot: A reference platform for robotics research and education," *IEEE Robotics & Automation Magazine*, vol. 29, no. 2, pp. 46–64, 2022.
- [24] K. Shankar, M. Tjersland, J. Ma, K. Stone, and M. Bajracharya, "A learned stereo depth system for robotic manipulation in homes," *IEEE Robotics and Automation Letters*, vol. 7, no. 2, pp. 2305–2312, 2022.